A simple low-loss broadband DNP probe at W-band

Mallory L. Guy, Lihuang Zhu, Chandrasekhar Ramanathan*

Department of Physics and Astronomy, Dartmouth College, Hanover NH 03755, USA

Abstract

Magnetic-field and microwave-frequency modulated DNP experiments have recently been shown to yield improved enhancements over conventional DNP techniques. The resulting increase in signal-to-noise ratios can lead to significantly shorter acquisition times in signal-limited multi-dimensional NMR experiments, and could pave the way to the study of even smaller sample volumes. In this paper we describe the design and performance of a low-loss broadband probe for microwave frequency and amplitude modulated DNP, that has been engineered to minimize both microwave and thermal losses during operation at liquid helium temperatures. The centerpiece of our strategy relies on a mode conversion from fundamental mode to a Gaussian mode outside of the cryostat then transmitting the microwaves down an overmoded brass pipe waveguide into the magnet. At the center of the magnetic field, the sample can either be placed inside the pipe or the microwaves can be re-converted back to fundamental mode. The microwave bandwidth of the probe is primarily determined by the final antenna or resonator used to excite the sample, and its coupling to the NMR RF coil. We have also built a longitudinally-detected EPR system based on the same microwave

*Corresponding author

Email address: sekhar.ramanathan@dartmouth.edu (Chandrasekhar Ramanathan)

excitation design. We demonstrate the utility of our design with a set of triangular frequency-modulated DNP experiments.

1. Introduction

Dynamic nuclear polarization (DNP) offers one route to overcoming the low detection sensitivity of NMR that has frequently limited its applicability, requiring either large sample volumes or long data acquisition times to attain acceptable signal-to-noise ratios. Recently, microwave-induced DNP has been applied to solid-state biomolecular spectroscopy at cryogenic temperatures [1, 2, 3, 4, 5, 6, 7, 8, 9]. Additionally dissolution DNP techniques [10] have enabled hyperpolarized solutions to be used for room-temperature studies in both process engineering [11] and biomedical applications [12, 13, 14, 15, 16, 17, 18]. The large spin polarizations have also enabled high temporal resolution studies of chemical processes [19], the use of novel ultra-fast multidimensional spectroscopy techniques [20], and could possibly allow extremely high-resolution magnetic resonance imaging [21].

The enhancements achieved in typical continuous wave (CW) DNP experiment are often as much as an order of magnitude lower than the theoretically predicted value of the ratio of the electron gyromagnetic ratio to the nuclear gyromagnetic ratio [22]. There are many factors that limit the enhancement observed in CW DNP experiments, such as imperfect microwave saturation caused by limited microwave power, inefficient excitation of a broad ESR line, and the presence of multiple DNP and leakage pathways. A number of efforts have been made to improve DNP enhancements by addressing each of these issues. Of particular note are the efforts to develop water soluble free radicals that optimize DNP enhancement at

high magnetic fields [23, 24, 25, 26]. Magnetic field modulation [28] and microwave frequency modulation [29, 30] have both been used to improve DNP enhancements by a factor of 2–3 by improving the saturation of broad ESR lines. While the presence of leakage relaxation pathways has long been known [22], the possibility of multiple (potentially competing) DNP pathways has recently also been pointed out [31, 32, 33]. Cory and co-workers have explored the use of optimal control techniques to improve pulsed DNP enhancements at low field [34], by selectively exciting a particular DNP pathway while suppressing leakage paths. These studies suggest that amplitude and frequency modulated microwave excitation schemes hold potential to improve the enhancements obtained in DNP experiments. However, these techniques also impose additional design constraints on the microwave transmission schemes used in DNP probe design.

In this paper we describe the design and performance of a low-loss broadband DNP probe that is compatible with both frequency and amplitude modulated DNP experiments. The probe described here is designed to fit inside a Janis STVP continuous flow cryostat, which fits in the bore of a 3.34 T ($\approx$ 94 GHz ESR frequency for $g \sim 2$) Oxford superconducting NMR magnet (100 mm superwide bore). In this system the magnet center is located 735 mm below the top flange of the magnet, and the top of the cryostat is 400 mm above the top flange of the magnet.

2. Millimeter-wave subsystem

2.1. Overview

One of the biggest challenges in designing a DNP probe is transmitting high frequency microwaves efficiently over long distances while simultaneously

minimizing thermal losses. There are many approaches to this, including the use of corrugated waveguides, standard over-moded waveguides, quasi-optical designs, and fundamental mode waveguides [28, 35, 36, 37, 38, 39, 40].

While thermal engineering is less critical for DNP experiments performed at liquid nitrogen temperatures, it is very important in the design of experiments at liquid helium temperatures. In general fundamental mode waveguide is the simplest scheme to set up, but there is a tradeoff between minimizing microwave and thermal losses (see Table 1). For example, copper waveguides minimize microwave losses but have the highest thermal losses, while stainless steel waveguides have high microwave losses but low thermal losses. Since the millimeter waves only propagate through a thin surface layer of the waveguide, gold or silver plating of a low-thermal conductivity metal such as stainless steel would seem a reasonable solution. However, it is typically difficult to gold- or silver-plate such narrow structures uniformly over the approximately one meter long length required.

The use of over-moded waveguide improves the microwave performance over fundamental mode. Since conventional over-moded waveguides are larger than fundamental mode waveguides, they have a higher thermal mass and thus present more of a problem with heat loss during experiments at liquid helium temperatures. Additionally, they may not be compatible with certain experimental set-ups because of space constraints. Corrugated waveguides are an alternative to over-moded waveguide, but they tend to be more expensive than fundamental mode and become harder to machine well at higher frequencies. Quasi-optical approaches to microwave transmission are perhaps the least lossy approach, but tend to be expensive, and designing and building such a set-up can be labor intensive. Additionally, there can be stability issues experienced with quasi-optical designs [41], since the compo-

Transmission scheme	W-band microwave loss (dB/m)	Thermal conductivity (W/m K)
Fundamental (copper)	2.59	380 - 390
Fundamental (silver coated)	2.59	406 - 418
Fundamental (stainless steel)	18.86	16 - 18
Over-moded (copper)	1-1.5	380 - 390
Corrugated (brass)	< 1	109 - 121
Quasi-optical designs	< 1	

Table 1: Summary of the loss and thermal conductivity of common methods of W-band microwave transmission [43, 41].

nents are sensitive to temperature. Decreases in microwave power delivered to DNP samples have been reported to be as high as 50% with an angular misalignment of just 0.1° [42]. Table 1 summarizes the loss experienced by each of these common types of transmission at W-band.

2.2. Proposed Design

Our experimental set-up is a relatively simple, cost-effective approach to balancing the competing requirements of microwave transmission and thermal efficiency, essentially employing a guided quasi-optical transmission system. The top of the microwave transmission setup is shown in Figure 1. The source is connected to a 24 inch (610 mm) section of gold-plated fundamental mode waveguide which extends over the center of the magnet (A). This is followed by a 90 degree E-plane bend which orients the waveguide along the axis of the magnet (B). After the 90 degree bend, the fundamental mode is converted to a gaussian mode using a scalar feed horn antenna (SFH-10-R0000 Millitech Inc.).

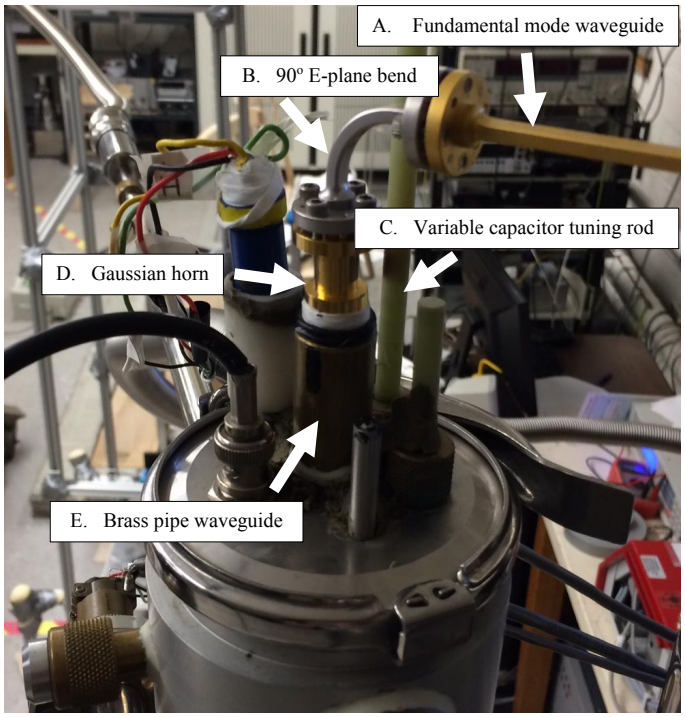

Figure 1: Top of our DNP microwave transmission, showing the 24-inch (610 mm) section of gold-plated fundamental mode waveguide which extends over the center of the magnet (A); the 90 degree E-plane bend which orients the waveguide along the axis of the magnet (B); the tuning rod for the variable capacitor used to tune the RF NMR coil (C); the gaussian horn used to convert from fundamental mode to a gaussian mode (D); and the brass pipe waveguide (E).

The output of the horn sits inside a thin-walled brass pipe (5/8-inch or 15.875 mm diameter, 0.05-inch or 1.27 mm wall thickness) which acts as an over-moded waveguide and extends down the length of the probe. The top of the brass pipe is sealed by a quartz window using an epoxy seal to isolate the interior of the cryostat during cryogenic experiments. The gaussian mode has an exponentially decaying profile that suppresses the fields (and

currents) at the wall of the waveguide, minimizing microwave losses. The thin-walled brass pipe also has a small thermal mass that limits heat losses. We estimate the thermal loss in our system to be similar to that of the corrugated brass waveguide in Table 1.

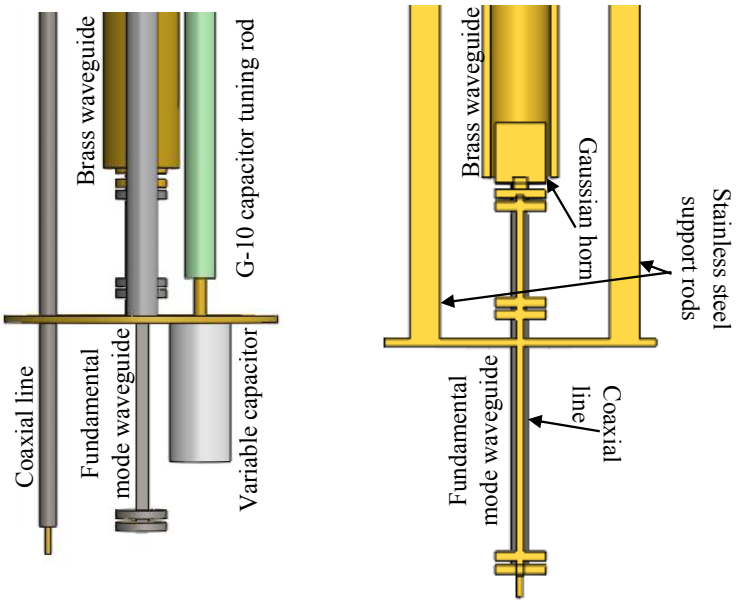

Figure 2: Side views of the bottom of the probe, showing the relative positions of the RF coaxial cable, the brass waveguide and the receiving gaussian horn, and the variable capacitor and tuning rod.

About 6 inches (152 mm) from the center of the magnetic field, the brass pipe ends and a receiving scalar horn antenna sits inside the brass pipe. This Gaussian horn re-converts the microwaves back to fundamental mode. The conversion back to fundamental mode is done to achieve better control of the orientation of the microwave magnetic field at the sample, as will be discussed in the next section. The receiving horn is followed by a short section ($\approx$ 4 inches or 101 mm) of fundamental mode waveguide that

extends to just above the NMR coil, as shown in Figure 2. At this waveguide flange it is possible to connect either a broad-band antenna such a standard pyramidal scalar gain antenna, or a resonant structure consistent with DNP measurements such as a Fabry Perot cavity [44] or a scroll resonator [45].

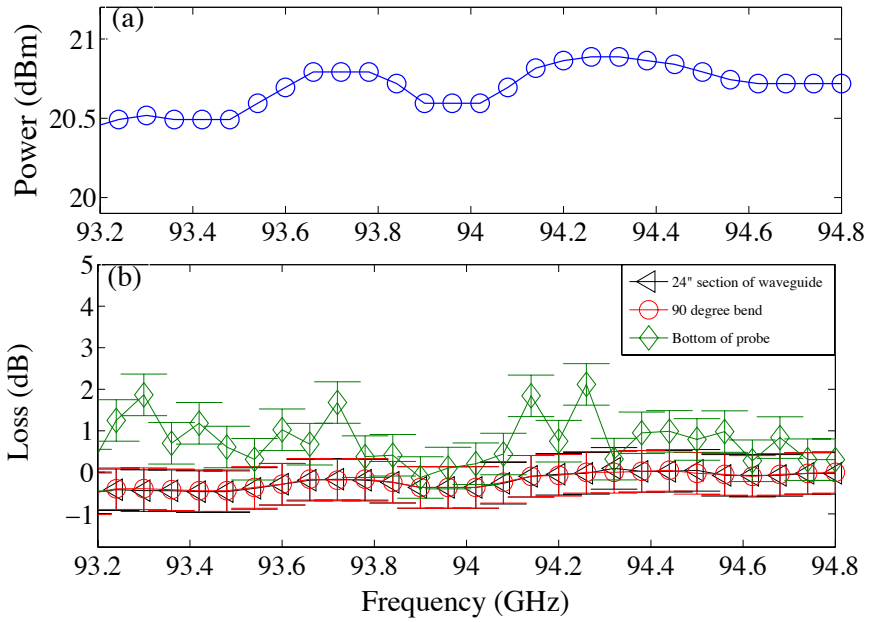

Figure 3: (a) Output power of the microwave source as a function of frequency. (b) Loss as a function of frequency for each stage of transmission down the DNP probe. The black triangles represent the loss after the 24" section of waveguide, the red circles represent the loss after the 90° bend, and the green diamonds represent the cumulative loss at the bottom of the probe.

2.3. Bandwidth and Loss Measurement

Our millimeter wave source covers the frequency range 90–96 GHz. Since our goal is to explore millimeter-wave frequency modulations in the range of ±1.5 GHz about the center frequency, which is comparable to the width of the broadest ESR linewidths and hyperfine interactions we expect to explore,

we measured the insertion loss at each stage of transmission using a W-band diode detector (Spacek DW-2P) in the 92–96 GHz frequency range.

First, the detector was connected directly the output of the microwave source to record the microwave power output by the source as a function of frequency (Figure 3a). The detector was then used to measure the microwave power as a function of frequency at three locations along the probe: at the end of the long section of the fundamental mode waveguide; after the 90 degree E-plane bend; and at the end of the receiving Gaussian horn at the bottom of the probe. Figure 3b shows the cumulative losses measured up to each of these locations. Losses along the fundamental mode waveguide and the 90 degree bend were found to be negligible in the frequency range measured.

The loss measurements of the brass overmoded waveguide were taken with the probe positioned vertically on a probe stand. In this configuration small adjustments and movements of the probe were observed to cause fluctuations in the measured power (indicated by the relatively large error bars). We note that this instability and fluctuation should be minimized when the probe is inside the magnet during experiments. Small movements can cause the Gaussian horns to shift relative to each other, and even a slight misalignment in the transmitting and receiving Gaussian horns can result in significant power loss. A future improvement to this transmission scheme would be the development of a better method of aligning the two horns.

The loss of the entire transmission scheme is typically less than 1 dB, including the mode-conversions and the long section of fundamental mode waveguide. It is important to note that this loss is dominated by the quartz window epoxied to the top of the brass pipe. When we repeated the measure-

ments using a brass tube that did not have a window, the transmission was observed to be almost lossless. The loss profile is approximately frequency independent over the range 93-95 GHz.

2.4. Microwave Sample Excitation

The antenna or cavity structure used to irradiate the sample depends on the coil and sample geometry used. This often tends to be the structure that ultimately limits the bandwidth of the system. Additionally, since only the microwave magnetic field components transverse to the main static field contribute to the excitation of the electron spins, it is important that the microwave power delivered down the probe is efficiently coupled to a mode that has such a transverse component.

We used Ansoft HFSS to perform a three-dimensional finite-element simulation of the three-dimensional distribution of the electromagnetic fields in two situations. The first is a simple pyramidal scalar gain horn system which is a simple broadband antenna that allows us to irradiate fairly large sample sizes; while the second explores the possibility of placing the sample inside the brass pipe to achieve improved microwave bandwidth, at the expense of limiting sample size. It should be noted that the Cory [47] and Han [48] groups have recently demonstrated that bandwidth restrictions are not a fundamental limitation in the design of complex microwave modulation schemes. A millimeter microwave resonator would also potentially permit regular ESR measurements in the same probe.

2.4.1. Pyramidal scalar gain horn

The spatial distribution of the microwave magnetic field for the pyramidal horn obtained by HFSS simulations is shown in Figure 4. The pyramidal

horn (2 cm by 2 cm). The field structure is mostly homogenous in a large area (approximately 1 cm wide), making this structure well-suited for studying surface samples such as monolayers and thin films. While simple, the pyramidal horn does show almost an 8 dB variation in the simulated S_{11} network parameter, showing its potential limits for broadband excitation. We also simulated the effects of including the NMR detection coil in the mode structure of the pyramidal horn. These simulations are shown in Figure 4. The NMR coil has a significant impact on the mode structure of the microwave magnetic field, resulting in an even larger variation in the simulated S_{11} parameter, though the fields are still relatively uniform in the coil.

2.4.2. Open pipe

Since the transmission down the probe was observed to be extremely broadband, we also examined the possibility of using the brass pipe to directly excite the sample. An HFSS simulation of the vector magnetic field structure of the Gaussian mode, both within the circular brass pipe and as it exits the pipe, is shown in Figure 5. Inside of the pipe, the field structure is perpendicular to the static field, which is ideal for DNP. However the spatially homogeneous part of the field is restricted to a small zone at the center of the pipe.

Outside of the pipe, the field structure starts to become significantly more complicated. The simulations show that the microwave magnetic field begins to pick up longitudinal components outside the pipe, which get progressively larger away from the edge of the pipe. While the magnitude of the field is slightly more homogeneous outside the pipe, the peak intensity is about a factor of three smaller than the maximum inside the pipe.

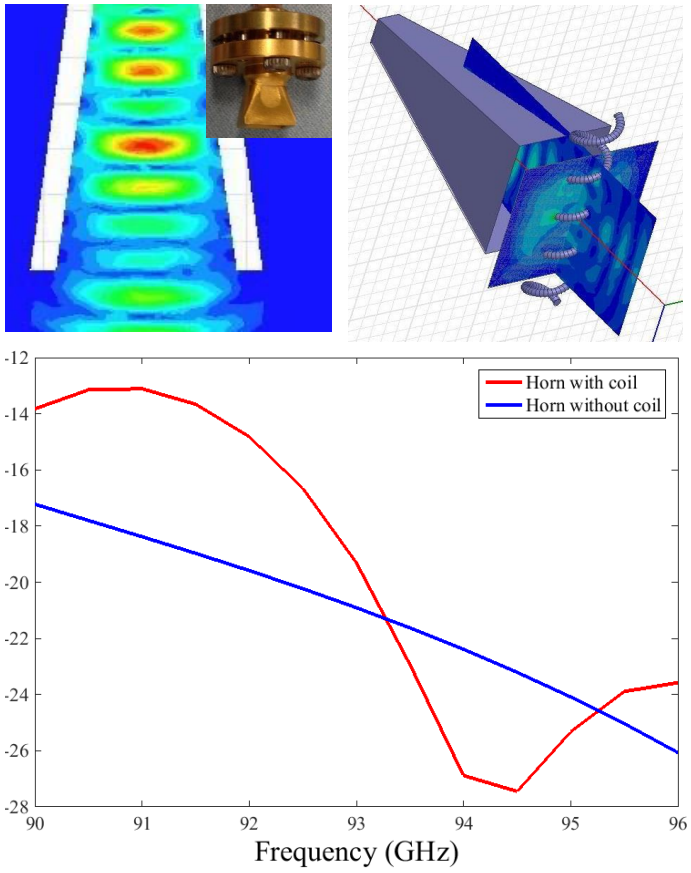

Figure 4: Microwave magnetic field distribution for the pyramidal horn without and with an NMR coil at 94 GHz. Simulated frequency dependence of the S_{11} network parameter.

195 For sufficiently small samples, it should be possible to position an NMR coil inside brass pipe to maintain broadband efficiency while being relatively unaffected by the spatial inhomogeneity of the field.

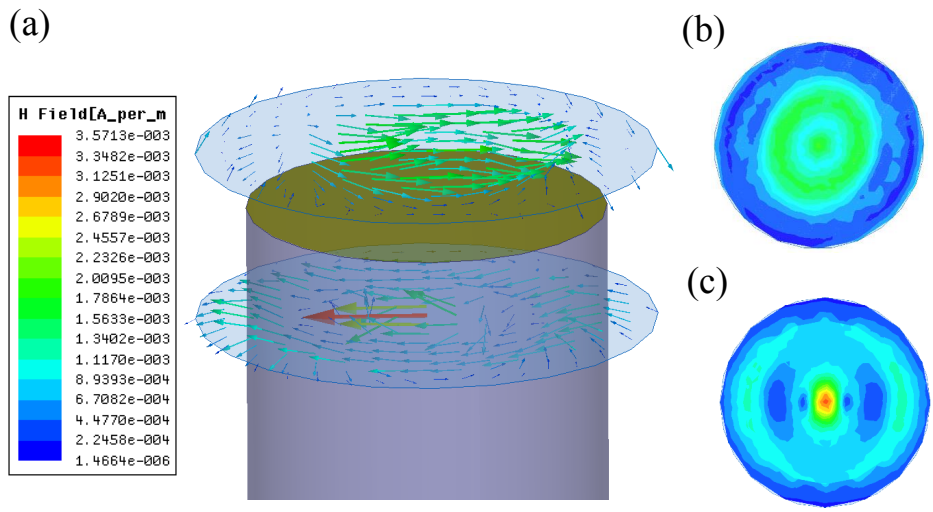

Figure 5: (a) HFSS simulations of the Gaussian mode structure, showing the vector magnitude of the microwave magnetic field in cross-sectional planes located inside and outside the brass pipe. (b) Cross section of the magnitude of the microwave magnetic field in a plane outside of the pipe. (c) Cross section of the magnitude of the microwave magnetic field in a plane inside of the pipe. The simulations were run at 94 GHz.

3. Other Features

3.1. NMR coil

The NMR detection circuit used to collect the data is a standard series-match parallel-tune resonance circuit [52]. A semi-rigid coaxial cable with stainless-steel outer conductor and a silver plated copper inner conductor (Micro-coax -UT-141-SS) connects the room temperature BNC connector to the tuned low-temperature circuit. The matching capacitor is a low temperature, fixed value capacitor (3 pF). The tunable capacitor is a ceramic, hermetically sealed capacitor (Voltronics NMTM120C) which has a range of 1–125 pF, and maintains tunability even at low temperatures. A G-10 rod with a tapered end fits into the tuning shaft of the tuning capacitor.

The rod extends the length of the probe, where it passes through a vacuum flange (Goddard Quikonnect valve). This allows tuning from outside of the cryostat, an important capability for low temperature experiments since the change in temperature from 300 K to 4 K causes the resonance to change appreciably.

3.2. Millimeter-wave source

Our source consists of a tunable phase-locked oscillator, combined with an x6 active multiplier that can output frequencies in the range of 87.6 to 98.4 GHz. This signal, which is set to about 90 GHz, is fed into the local oscillator (LO) port of a balanced mixer. The intermediate frequency (IF) port on the mixer has a bandwidth of 4-5 GHz, which is where we can input a modulated 4 GHz signal. The output of the mixer is passed through an iris filter with a 4 GHz bandwidth that filters out the lower side band at 86 GHz, and is passed to a 200 mW high power amplifier. The signal is then passed through a voltage controlled variable attenuator (20 dB max) that can be used for gating the pulses, or additional modulation.

In order to implement frequency modulated DNP, we mix the output of a constant 2 GHz oscillator with a frequency modulated signal generated by an arbitrary waveform generator (AWG) and after appropriate filtering, input this to the IF port of the millimeter wave mixer. A schematic of the source is shown in Figure 6.

3.2.1. LOD-EPR Detection

We also adapted the above design to implement LOD EPR measurements using the scheme proposed by Granwehr *et al.* [49]. A separate probe was used for convenience to avoid having to switch coils. The RF coil described above is replaced by an un-tuned pick-up coil with 12 turns directly

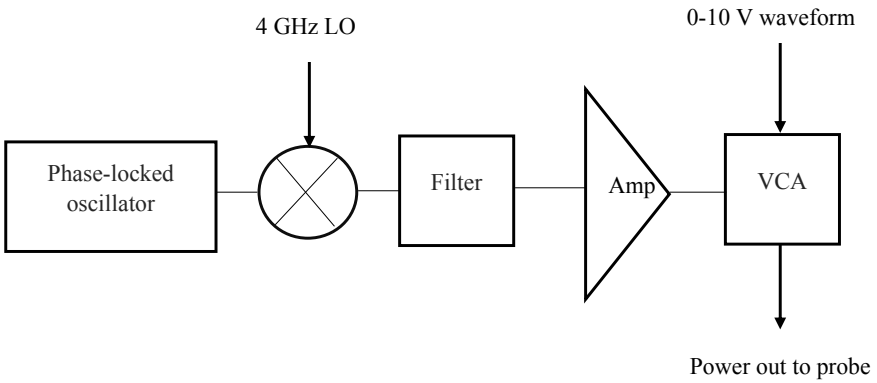

Figure 6: Block diagram of microwave source used in the frequency modulated experiments.

below the microwave horn, at the center of the magnetic field. The voltage-controlled attenuator is used to amplitude modulate the microwaves in an on-off scheme for performing LOD experiments. This on-off microwave modulation is performed on the order of the electronic T_1 of the sample. The microwave frequency is swept, and the spins generate an EMF in a pick-up coil oriented parallel to the static magnetic field. The signal is detected via a lock-in amplifier.

4. Experimental Results

4.1. CW DNP

To demonstrate the performance of our probe, we ran CW DNP experiments on a standard sample of 40 mM solution of 4-amino TEMPO in a 60:40 glycerol-water mixture. The sample was degassed using a freeze-pump-thaw cycle which was repeated three times. This was done to remove dissolved paramagnetic oxygen to reduce relaxation pathways and provide a nuclear

relaxation time long enough to see significant DNP enhancement.

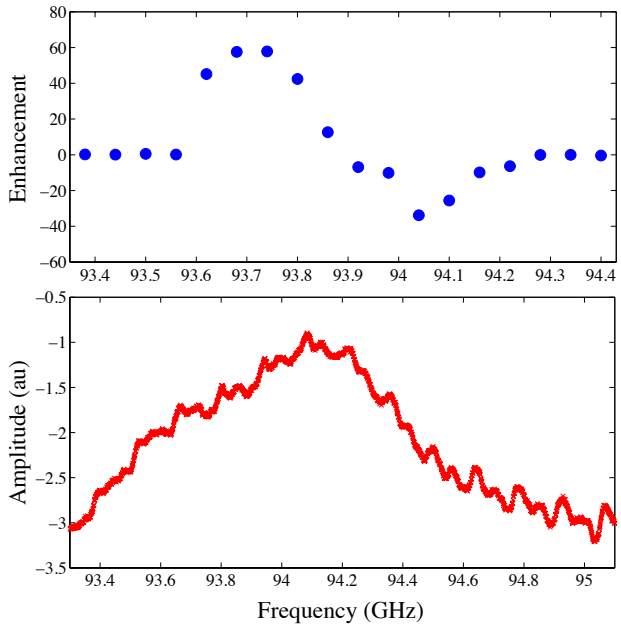

Figure 7: (Above) Experimental frequency swept proton DNP data for the pyramidal horn with a 40 mM solution of 4-amino TEMPO in a 60:40 glycerol-water mixture. Error bars are smaller than the size of the symbols used. (Below) The longitudinally-detected EPR signal for a 10 mM solution of TEMPO system.

Figure 7 shows the DNP enhancement observed at 4 K as a function of microwave excitation frequency using the pyramidal horn. The strength of the signal in each experiment was estimated by averaging the first 10 points of the real channel of the FID. Errors were estimated using the standard deviation of the noise, which was taken to be the last 25 points in the time domain data (a signal-free region). The experiments were performed in a 3.3 T field using a Bruker DRX spectrometer. The $\pi/2$ pulse in this experiment is approximately 1.5 μs. The maximum DNP enhancement occurs at 93.83 GHz, and is 57.81 $\pm$0.228.

The figure also shows the LOD-EPR signal from a 10 mM solution of the TEMPO system. The microwave amplitude modulation frequency was 25 kHz, and the experiment was performed at liquid nitrogen temperatures. The pick-up coil used is significantly larger than the NMR coil, which contributes to the significantly broader EPR line compared to the frequency range over which DNP was observed. As discussed previously, we believe that the frequency response of the horn-coil system in the DNP probe is another factor that contributes to the difference in the observed frequency response.

4.2. Frequency modulated DNP

We performed preliminary triangular frequency-modulated DNP experiments to demonstrate the capabilities of the system. Figure 8a shows the parameters used in triangular frequency modulated DNP. There is a center frequency, ω_0 and a step, $\delta\omega$, which is the size of the region swept above and below the center frequency. The triangular modulation is performed at a specified modulation frequency, f_m. The modulated microwave output was produced by first mixing the output of a voltage controlled oscillator operating at about 1 GHz with a 3 GHz carrier, and then mixing the upper sideband of the resulting signal with the 90 GHz carrier described previously.

Figure 8b shows our experimental results comparing the NMR signals in the absence of DNP, CW DNP, and several different triangular modulated DNP experiments. The modulation data was taken with a $\delta\omega$ of 17.5 MHz, and a center frequency of 93.76 GHz. We performed the modulated DNP experiments at three modulation frequencies: 1 kHz, 10 kHz, and 100 kHz. We observed an improvement in the DNP enhancement from about 58 for CW DNP to about 169 for frequency modulated DNP in this sample, in

general agreement with the previous work [29].

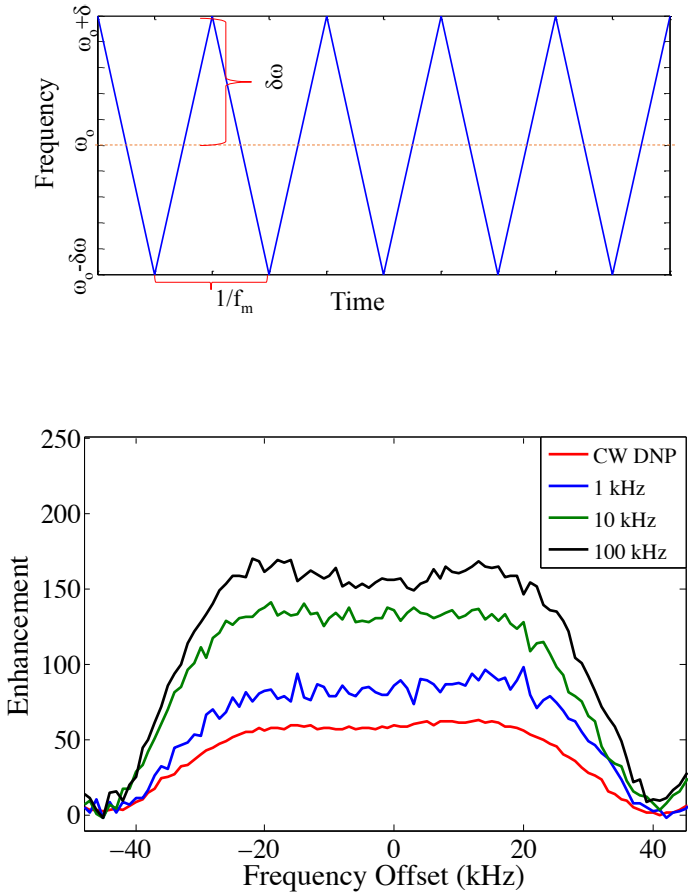

Figure 8: (a) Triangular frequency modulation used in frequency modulated DNP experiments, (b) Experimental data for triangular frequency modulated DNP on a 40 mM sample of TEMPO in a 60:40 mixture of glycerol:water.

5. Conclusion

We have demonstrated a low-loss, broadband, microwave transmission scheme for W-band DNP at cryogenic temperatures. The microwave bandwidth of the probe is limited primarily by the antenna or resonator used to couple the

microwaves to the sample, while the small microwave loss observed is dominated by the quartz window used to seal the brass pipe used as a waveguide. We also demonstrated the use of this scheme for both longitudinally-detected EPR as well as triangular frequency modulated DNP experiments.

Potential improvements include a better system or aligning the horns at the top and bottom of the cryostat to ensure the system is always in its lowest-loss configuration. Additionally, microwave losses could be reduced even further by using a lower loss material for window seal. We are currently exploring different antenna-coil configurations that maintain the broadbandedness of the system while maximing the coupling between the fields and the sample. Such a probe will be be invaluable for the systematic exploration of modulation schemes to improve DNP enhancement. For example, it would be very interesting to use our broadband, high field DNP probe to try to extend some of the ideas performed at low field to higher field, such as the application of optimal control theory of DNP [34].

6. Acknowledgements

This material is based in part upon work supported by the National Science Foundation under CHE-1410504. The setup used to measure the LOD-EPR spectrum shown was funded by the Pilot Project Program of the Dartmouth Physically Based Center for Medical Countermeasures Against Radiation, with NIH funding from the National Institute of Allergy and Infectious Diseases (U19-AI091173). The authors would also like to thank Whitey Adams and Chris Grant for machining various components of our set-ups and Leon from Aerowave for helpful discussions.

7. References

[1] D.A. Hall, D.C. Macus, G.J. Gerfen, S.J. Inati, L.R. Becerra, F.W. Dahlquist, R.G. Griffin, Polarization-enhanced NMR spectroscopy of biomolecules in frozen solution, *Science*, **276**, 930–932 (1997).

[2] P. C. A. van der Wel, K. H. Hu, J. Lewandowski, R. G. Griffin, Dynamic nuclear polarization of amyloidogenic peptide nanocrystals: GNNQQNY, a core segment of the yeast prion protein Sup35p, *J. Am. Chem. Soc.*, **128**, 10840 (2006).

[3] T. Maly, G. T. Debelouchina, V. S Bajaj, K.-N. Hu, C.-G. Joo, M. L. Mak-Jurkauskas, J. R. Sirigiri, P. C. A van der Wel, J. Herzfeld, R. J. Temkin, R. G. Griffin, Dynamic nuclear polarization at high magnetic fields, *J. Chem. Phys.*, **128**, 052211 (2008).

[4] M. Mak-Jurkauskas, V. Bajaj, M. Hornstein, M. Belenky, R.G. Griffin, J. Herzfeld, Energy transformations early in the bacteriorhodopsin photocycle revealed by DNP-enhanced solid state NMR, *Proc. Natl. Acad. Sci. USA*, **105**, 883–888 (2008).

[5] V.S. Bajaj, M.L. Mak-Jurkauskas, M. Belenky, J. Herzfeld, R.G. Griffin, Functional and shunt states of bacteriorhodopsin resolved by 250 GHz dynamic nuclear polarization-enhanced solid state NMR, *Proc. Natl. Acad. Sci. USA*, **106**, 9244–9249 (2009).

[6] E. Salnikov, M. Rosay, S. Pawsey, O. Ouari, P. Tordo, B. Bechinger, Solid-state NMR spectroscopy of oriented membrane polypeptides at 100 K with signal enhancement by dynamic nuclear polarization, *J. Am. Chem. Soc.*, **132**, 5940–5941 (2010).

[7] I. Sergeyev, L. Day, A. Goldbourt, A. McDermott, Chemical shifts for the unusual DNA structure in Pf1 bacteriophage from dynamic-nuclear-polarization-enhanced sold-state NMR spectroscopy, *J. Am. Chem. Soc.*, **133**, 20208–20217 (2011).

[8] T. Jasco, T. Franks, H. Rose, U. Fink, J. Broecker, S. Keller, H. Oschkinat, B. Reif, Characterization of membrane proteins in isolated native cellular membranes by dynamic nuclear polarization solid-state NMR spectroscopy without purification and reconstitution, *Angew. Chem. Int. Edit.*, **51**, 432–435 (2012).

[9] A. Potapov, W.-M. Yau, R. Tycko, Dynamic nuclear polarization-enhanced 13C NMR spectroscopy of static biological solids, *J. Magn. Reson.*, **231**, 5-14 (2013).

[10] J. H. Ardenkjaer-Larsen, B. Fridlund, A. Gram, G. Hansson, L. Hansson, M.H. Lerche, R. Servin, M. Thanning, K. Golman, Increase in signal-to-noise ratio of $>$ 10,000 times in liquidstate NMR, *Proc. Natl. Acad. Sci. USA*, **100**, 10158–10163 (2003).

[11] E. R. McCarney, B. D. Armstrong, M. D. Lingwood, S. Han, Hyperpolarized water as an authentic magnetic resonance imaging contrast agent. *Proc. Natl. Acad. Sci. USA*, **104**, 1754–1759 (2007).

[12] K. Golman, R. in't Zandt, M. Lerche, R. Pehrson and J.H. Ardenkjaer-Larsen, Metabolic Imaging by Hyperpolarized 13C Magnetic Resonance Imaging for In Vivo Tumor Diagnosis, *Cancer Res.*, **66**, 10855 (2006).

[13] S.E. Day, M.I Kettunen, F.A. Gallagher, D.-E. Hu, M. Lerche, J. Wolber, K. Golman, J.H. Ardenkjaer-Larsen, and K.M. Brindle, Detecting

tumour response to treatment using hyperpolarized 13C magnetic resonance imaging and spectroscopy, *Nat. Med.*, **13**, 1382–1387 (2007).

[14] F.A. Gallagher, M.I. Kettunen, S.E. Day, D.-E. Hu, J.H. Ardenkjr-Larsen, R. in't Zandt, P.R. Jensen, M. Karlsson, K. Golman, M.H. Lerche, and K.M. Brindle, Magnetic resonance imaging of pH in vivo using hyperpolarized 13C-labeled bicarbonate, *Nature*, **453**, 940–943 (2008).

[15] F.A. Gallagher, M.I, Kettuenen, , D.-E. Hu, P.R. Jensen, R. in ?t Zandt, M. Karlsson, A. Gisselsson, S. K. Nelson, T.H. Witney, S.E. Bohndiek, G. Hansson, T. Peitersen, M.H. Lerche, and K.M. Brindle, Production of hyperpolarized [1,4-13C2]malate from [1,4-13C2]fumarate is a marker of cell necrosis and treatment response in tumors, *Proc. Natl. Acad. Sci. USA*, **106**, 19801–19806 (2009).

[16] J. Kurhanewicz, D.B. Vigneron, K. Brindle, E.Y. Chekmenev, A. Comment, C.H. Cunningham, R.J. Deberardinis, G.G. Green, M.O. Leach, S.S. Rajan, R.R. Rizi, B.D. Ross, W.S. Warren, and C.R. Malloy, Analysis of cancer metabolism by imaging hyperpolarized nuclei: prospects for translation to clinical research, *Neoplasia*, **13**, 81–97 (2011).

[17] M.C. Cassidy, H.R. Chan, B.D. Ross, P.K. Bhattacharya, C.M. Marcus, In vivo magnetic resonance imaging of hyperpolarized silicon particles, *Nat. Nanotechnol.*, **8**, 363–368 (2013).

[18] S.J. Nelson, J. Kurhanewicz, D.B. Vigneron, P.E. Larson, A.L. Harzstark, M. Ferrone, M. van Criekinge, J.W. Chang, R. Bok, I. Park, G. Reed, L. Carvajal, E.J. Small, P. Munster, V.K. Weinberg, J.H. Ardenkjaer-Larsen, A.P. Chen, R.E. Hurd, L.I. Odegardstuen, F.J.

Robb, J. Tropp, J.A. Murray, Metabolic Imaging of Patients with Prostate Cancer Using Hyperpolarized [1-13C]Pyruvate, *Sci. Transl. Med.*, **14**, 198 (2013).

[19] S. Bowen, C. Hilty, Time-resolved dynamic nuclear polarization enhanced NMR Spectroscopy, *Angew. Chem. Int. Edit.*, **47**, 5235–5237 (2008).

[20] L. Frydman,D. Blazina, Ultrafast two-dimensional nuclear magnetic resonance spectroscopy of hyperpolarized solutions. *Nat. Phys.*, **3**, 415–419 (2007).

[21] K. R.Thurber, R. Tycko, Prospects for sub-micron solid state nuclear magnetic resonance imaging with low-temperature dynamic nuclear polarization. *Phys. Chem. Chem. Phys.*, **12**, 5779–5785 (2010).

[22] A. Abragam and M. Goldman, Principles of dynamic nuclear polarisation, *Rep. Prog. Phys.*, **41**, 395–467 (1978).

[23] S. Macholl, H. Johannesson, J. H. Ardenkjaer-Larsen, Trityl biradicals and 13C dynamic nuclear polarization, *Phys. Chem. Chem. Phys.* **12** 5804–5817 (2010) .

[24] C. Song, K. N. Hu, C. G. Joo, T. M. Swager, R. G. Griffin, TOTAPOL: a biradical polarizing agent for dynamic nuclear polarization experiments in aqueous media, *J. Am. Chem. Soc.*, **128**, 11385–11390 (2006).

[25] Y. Matsuki, T. Maly, O. Ouari, H. Karoui, F. Le Moigne, E. Rizzato, S. Lyubenova, J. Herzfeld, T. Prisner, P. Tordo, R. G. Griffin, Dynamic nuclear polarization using a rigid biradical, *Angew. Chem. Int. Edit.*, **48**, 4996–5000 (2009).

[26] C. Sauvée, M. Rosay, G. Casano, F. Aussenac, R. T. Weber, O. Ouari and P. Tordo, Highly Efficient, Water-Soluble Polarizing Agents for Dynamic Nuclear Polarization at High Frequency, *Angew. Chem. Int. Edit.*, **52**, 10858–10861 (2013).

[27] A. Zagdoun, G. Casano, O. Ouari, M. Schwarzwälder, A. J. Rossini, F. Aussenac, M. Yulikov, G. Jeschke, C. Copéret, A. Lesage, P. Tordo and L. Emsley, *J. Am. Chem. Soc.*, **135**, 12790–12797 (2013).

[28] K. R. Thurber, W.-M. Yau, R. Tycko, Low-temperature dynamic nuclear polarization at 9.4 Tesla with a 30 milliwatt microwave source, *J. Magn. Reson.*, **204**, 303–313 (2010).

[29] Y. Hovav, A. Feintuch, S. Vega, D. Goldfarb, Dynamic nuclear polarization using frequency modulation at 3.34 T, *J. Magn. Reson.*, **238**, 94–105 (2014).

[30] A. Bornet, J. Milani, B. Vuichoud, A. J. Perez Linde, G. Bodenhausen, S. Jannin, Microwave frequency modulation to enhance dissolution dynamic nuclear polarization, *Chem. Phys. Lett.*, **602**, 63–67 (2014).

[31] D. Banerjee, D. Shimon, A. Feintuch, S. Vega, D. Goldfarb, The Interplay between the Solid Effect and the Cross Effect Mechanisms in Solid State 13C-DNP at 95 GHz Using Trityl Radicals, *J. Magn. Reson.*, **230**, 212-219 (2013).

[32] D. Shimon, A. Feintuch, D. Goldfarb, S. Vega, Static 1H dynamic nuclear polarization with the biradical TOTAPOL: a transition between the solid effect and the cross effect, *Phys. Chem. Chem. Phys.*, **16**, 6687-6699 (2014)

[33] T. V. Can, M. A. Caporini, F. Mentink-Vigier, B. Corzilius, J. J. Walish, M. Rosay, W. E. Maas, M. Baldus, S. Vega, T. M. Swager, R. G. Griffin, Overhauser effects in insulating solids, *J. Chem. Phys.*, **141** 064202 (2014).

[34] S. Sheldon, Optimal control in an open quantum system : selecting DNP pathways in an electron-nuclear system, Ph.D. thesis, MIT (2013).

[35] H. Cho, J. Baugh, C. A. Ryan, D. G. Cory, C. Ramanathan, Low temperature probe for dynamic nuclear polarization and multiple-pulse solid-state nmr, *J. Magn. Reson.*, **187**, 242–250 (2007).

[36] E. de Rijk, A. Macor, J.-P. Hogge, S. Alberti, J.-P. Ansermet, Note: Stacked rings for terahertz wave-guiding, *Rev. Sci. Instr.*, **82**, 066102 (2011).

[37] P. P. Woskov, V. S. Bajaj, M. K. Hornstein, R. J. Temkin, R. G. Griffin, Corrugated waveguide and directional coupler for cw 250-GHz gyrotron DNP experiments, *IEEE T. Microw. Theory*, **53**, 1863–1869 (2005).

[38] A. B. Barnes, E. A. Nanni, J. Herzfeld, R. G. Griffin, R. J. Temkin, A 250 GHz gyrotron with a 3 GHz tuning bandwidth for dynamic nuclear polarization, *J. Magn. Reson.*, **221** 147–153 (2012).

[39] B. D. Armstrong, D. T. Edwards, R. J. Wylde, S. A. Walker, S. Han, A 200 GHz dynamic nuclear polarization spectrometer, *Phys. Chem. Chem. Phys.*, **12** 5920–5926 (2010).

[40] K. J. Pike, T. F. Kemp, H. Takahashi, R. Day, A. P. Howes, E. V. Kryukov, J. F. MacDonald, A. E. C. Collis, D. R. Bolton, R. J. Wylde, M. Orwick, K. Kosuga, A. J. Clark, T. Idehara, A. Watts, G. M. Smith,

M. E. Newton, R. Dupree, M. E. Smith, A spectrometer designed for 6.7 and 14.1 T DNP-enhanced solid-state MAS NMR using quasi-optical microwave transmission, *J. Magn. Reson.* **215** 1–9 (2012).

[41] E. A. Nanni, S. K. Jawla, M. A. Shapiro, P. P. Woskov, R. J. Temkin, Low-loss transmission lines for high-power terahertz radiation, *J. Infrared Millim. W.*, **33**, 695–714 (2012) .

[42] B.D. Armstrong, D.T. Edwards, R.J. Wylde, S.A. Walker, S. Han, A 200 GHz dynamic nuclear polarization spectrometer, *Phys. Chem. Chem. Phys.*, **12**, 2010.

[43] T. Moreno, *Microwave Transmission Design Data*, Dover Publications, Inc., New York, 1958.

[44] D. J. Singel, H. Seidel, R. D. Kendrick, C. S. Yannoni, A spectrometer for EPR, DNP, and multinuclear high-resolution NMR, *J. Magn. Reson.* **81**, 145–161 (1989).

[45] V. Weis, M. Bennati, M. Rosay, J. A. Bryant, R. G. Griffin, High-field DNP and ENDOR with a novel multiple-frequency resonance structure, *J. Magn. Reson.*, **140**, 293–299 (1999).

[46] V. Denysenkov, T. Prisner, Liquid state dynamic nuclear polarization probe with fabry–perot resonator at 9.2 T, *J. Magn. Reson.*, **217**, 1–5 (2012).

[47] T. W. Borneman and D. G. Cory, Bandwidth-limited control and ring-down suppression in high-Q resonators, *J. Magn. Reson.*, **225**, 120-129 (2012).

[48] T. Kaufmann, T. J. Keller, J. M. Franck, R. P. Barnes, S. J. Glaser, J. M. Martinis, S. Han, DAC-board based X-band EPR spectrometer with arbitrary waveform control, *J. Magn. Reson.*, **235**, 95–108 (2013).

[49] J. Granwehr, J. Leggett, and W. Köckenberger, A low-cost implementation of EPR detection in a dissolution DNP setup, *J. Magn. Reson.*, **187**, 266–276 (2007).

[50] O. Grinberg, L. Berliner, Very High Frequency (VHF) ESR/EPR, 1st Edition, No. 22 in *Biological Magnetic Resonance*, Springer, 2004.

[51] M. C. Cassidy, Hyperpolarized silicon particles as in-vivo imaging agents, Ph.D. Thesis, Harvard University (2012).

[52] E. Fukushima and S. B. W. Roeder, *Experimental Pulse NMR: A Nuts and Bolts Approach*, Westview Press, 1993.